Computational Geosciences (2020) 24:1523–1539
https://doi.org/10.1007/s10596-020-09941-w

ORIGINAL PAPER

Rapid estimation of permeability from digital rock using 3D convolutional neural network

Jin Hong[1] · Jie Liu[1]

Received: 16 September 2019 / Accepted: 4 February 2020 / Published online: 27 May 2020

Abstract

Permeability and its anisotropy are of central importance for groundwater and hydrocarbon migration. Existing fluid dynamics methods for computing permeability have common shortcomings, i.e., high computational complexity and long computational time, reducing the potential of these methods in practical applications. In view of this, a 3D CNN-based approach for rapidly estimating permeability in anisotropic rock is proposed. Using high-resolution X-ray microtomographic images of a sandstone sample, numerous samples of the size of 100-cube voxels were generated firstly by a series of image manipulation techniques. The shrinking and expanding algorithms are employed as the data augmentation methods to strengthen the role of porosity and specific surface area (SSA) since these two parameters are critical to estimate permeability. Afterwards, direct pore-scale modeling with Lattice-Boltzmann method (LBM) was utilized to compute the permeabilities in the direction of three coordinate axes and mean permeability as the ground truth. A dataset including 3158 samples for training and 57 samples for testing were obtained. Four 3D CNN models with the same network structure, corresponding to permeabilities in 3 directions and in average, were built and trained. Based on those trained models, the satisfactory predictions of the permeabilities in x-, y-, and z-axis directions and the mean permeability were achieved with R^2 scores of 0.8972, 0.8821, 0.8201, and 0.9155, respectively. Furthermore, those proposed 3D CNN models achieved good generalization ability in predicting the permeability of other samples. The trained model takes only tens of milliseconds on average to predict the permeability of one sample in one axial direction, about 10,000 times faster than LBM. The promising performance clearly demonstrates the effectiveness of 3D CNN-based approach in rapidly estimating permeability in anisotropic rock. This new approach provides an alternative way to calculate permeability with low computing cost, and it has the potential to be extended to the estimation of relative permeability and other properties of rocks.

Keywords Anisotropic rock · Digital rock physics · Permeability estimation · 3D convolutional neural network · Shrinking and expanding

1 Introduction

All the time understanding fluid flow and mass transport in porous media is crucial to geological and engineering applications, e.g., contaminant remediation, building stone performance, oil recovery, hydrology, CO_2-sequestration, and geothermal energy generation. Permeability is the key parameter to understanding fluid flow. The measurement of permeability includes laboratory experiments, empirical estimation, direct pore-scale modeling, and pore network models. The latter two methods are based on digital rock images, such as microtomography (microCT) and focused ion beam (FIB) images, with detailed pore structures at microscale [1–4]. We propose to estimate permeability by using 3D convolutional neural network (CNN) based on digital rock images, and this would become another approach of permeability estimation with certain advantages.

Direct pore-scale modeling contains lattice-Boltzmann method (LBM), traditional mesh-based computational fluid dynamics method (including finite difference method, finite volume method, and finite element method), smoothed particle hydrodynamics, direct hydrodynamics, and molecular dynamics method [5–10]. Direct approach aims at solving the Navier-Stokes equations (or its simplification) directly on the

✉ Jie Liu
liujie86@mail.sysu.edu.cn

Jin Hong
hongj5@mail2.sysu.edu.cn

[1] School of Earth Sciences and Engineering, Sun Yat-Sen University, Guangzhou 510275, China

3D geometry of pore with complex boundary conditions. With taking all structure details of the pore space into account, direct pore-scale modeling has been regarded as the most accurate approach, but the computational burden is very heavy, especially for simulating multiphase flows and reactive transport [11, 12]. Extremely high computational cost limits the geometry size of numerical simulation in most applications to a very small. Furthermore, meshing networks manually in direct approach is complicated usually.

Pore-scale modeling with pore network models simplifies the complex pore space into a network containing pore bodies and pore throats with regular shapes, e.g., cylinder, sphere, and then simulate the flow and transport processes using related and simplified laws on the simpler network [4, 13]. Although pore-scale modeling with pore network models can reduce computational demands, making this approach more broadly used in simulations of multiphase flow and transport in geological field [1, 14], the simplified network cannot completely replicate the real topology of complex porous media which is crucial for transport behavior [15, 16]. Moreover, due to the differences in understanding of the pore body and pore throat, the network structures extracted by different researchers are different, leading to biases in later interpretation.

Permeability depends only on the pore structure inside the rock. Kozeny-Carman equation [17, 18], a semi-empirical formula, gives good agreement of estimated permeability of porous media with laboratory experiments and is widely used in the field of fluid flow. However, parameters such as tortuosity and Kozeny-Carman constant are various from sample to sample and require additional steps to approximate [19, 20]. The determination of these parameters may be complex and with uncertainty. The essential idea of Kozeny-Carman equation is that there is a mapping (or function) between several artificially designed features based on the 3D geometry of pore space and the permeability value. Obviously, this function is considered very complex and difficult to acquire.

However, previous studies suggested that complex mapping functions could be approximated by deep neural networks (DNNs) according to the universal approximation theorem (UAT) and its variants [21–24]. As an extension of DNNs, except for fully connected layer, convolutional neural network (CNN) includes convolution layer which is employed to extract task-related features automatically. Currently, CNN and its variants have achieved great success in many fields, such as medical image segmentation and focus diagnosis [25–29], face recognition [30–32], prediction of multiphase material properties [33–35], and digital rock physics [36–38]. CNN is generally divided into 2D CNN and 3D CNN according to dimension size. At present, 2D CNN is the most widely used, because 3D CNN need expensive computational cost, memory requirement, and time consumption [39, 40]. However, 3D CNN has a natural advantage in processing 3D data since it can take full advantage of the volumetric contextual information in all three dimensions [41]. 3D CNN has been used in 3D action recognition [42], 3D medical image segmentation [39], speech emotion recognition [43], and so on. In terms of permeability prediction, Wu et al. [37] developed a physics-informed 2D CNN as the surrogate model for predicting permeability in 2D isotropic porous media generated using a Voronoi tessellation algorithm [44–46]. Sudakov et al. [38] performed a preliminary study on predicting permeability of Berea sandstone using several machine learning methods. They evaluated those methods and concluded that the 3D CNN was the best.

However, the models in Wu's study [37] is based on the artificial 2D porous media which is not applicable because (i) natural porous media are 3D and much more complex; (ii) the connectivity or percolation of pores may be totally different in 3D and 2D spaces for the same porosity [47]. Permeability anisotropy, which is crucial to groundwater and hydrocarbon migration because of the strong influence on the direction fluids propagate, was not taken into account in Sudakov's research [38]. Based on our research experience, the voxel cubes with size of $100 \times 100 \times 100$ employed in their study should have anisotropy generally. Furthermore, the method used to compute the permeability in their paper is pore-scale modeling with pore network models, which cannot make full use of the information of each pixel of the three-dimensional rock digital image, and its accuracy is inferior to that of direct pore-scale modeling.

In this paper, we propose to use 3D CNN to estimate permeability in natural rock with taking permeability anisotropy into account. In generating experimental samples, a special data augmentation technique (shrinking and expanding algorithms [48, 49]) was employed for strengthening the role of porosity and specific surface area (SSA) instead of introducing physics-informed CNN [37]. To train and test our models, Lattice-Boltzmann method (LBM), a commonly used direct pore-scale modeling with good accuracy, is utilized to compute the permeabilities in the direction of three coordinate axes and the mean permeability used as the indicator for evaluating the overall flow and transport properties of rock. Corresponding to the permeabilities in 3 directions and in average, four 3D CNN-based models are built, and then trained with the obtained dataset. Based on those trained models, satisfactory predictions on all kinds of permeability are obtained.

2 Methodology and dataset

2.1 Overview of research plan

In order to achieve a 3D CNN-based approach for fast estimation of anisotropic permeability, we designed a research plan

as shown in Fig. 1, which involves 3 major steps of (i) building datasets, (ii) training 3D CNN models, and (iii) evaluating trained models. Details are given in the following.

(i) Building datasets including training data and test data

We first generate a large number of 3D binary images representing pore geometry after performing a series of image operations and separate then into two sets. One set is used for training the 3D CNN models, and the other for testing. Direct pore-scale modeling with LBM is performed on both sets of images for computing the permeabilities in three axial directions (K_x, K_y, K_z) and the mean permeability (K_m) as the ground truth in this study (Fig. 1a). The images labeled with four kinds of permeability make up the dataset of our experiment. More details about building dataset are presented in Section 2.2.

(ii) Training 3D CNN models with training data

In this step, we design four 3D convolutional neural networks for corresponding to four kinds of permeability. The training data generated in previous step are used to train those 3D CNN models. For each model, as shown in Fig. 1b, the 3D binary image is inputted into the model and the permeability is outputted. The weights of the model are adjusted so that the output (K'_x, K'_y, K'_z, K'_m) can be as close as possible to the ground truth (K_x, K_y, K_z, K_m). See Section 2.3 for more details about 3D CNN.

(iii) Evaluating the trained models with test data

The test data obtained from step (i) are used to test the four trained models. For each model, the permeability was estimated rapidly with inputting the image into the corresponding model, and the obtained permeability is validated with the ground truth for evaluating the trained model (see Fig. 1c). The results of evaluation are presented in Sections 3.3 and 3.4.

2.2 Dataset acquisition

In this study, a Coconino sandstone representing medium-porosity sandstone was employed for our experiments. The Coconino sandstone is an early Permian eolian rock with 96% quartz, 2% feldspar, and 2% iron oxide and clay and it was obtained from a quarry in northern Arizona [50]. A cylindric specimen cut out from the Coconino sandstone was X-ray CT scanned with the resolution of 1.995 μm. A series of operations on this specimen were performed successively for acquiring dataset as shown in Fig. 2.

(i) Image processing

Firstly, the original greyscale image with a minimum gray value of 6680 and a maximum gray value of 65,535 was loaded and a cube of 600 voxel in side-length was cropped from the cylindric specimen area. No artifacts were found in the cube of 600 voxel after we examined the slices one by one. Median filter with 3D interpretation was used to filtrate the noisiness in the 3D greyscale image. Afterwards, the gray value of 13,000 was selected as the appropriate threshold to segment the voxel cube for extracting the pore geometry. At last, a 3D binary volume representing the pore geometry was obtained. Based on this binary image, the number of voxels denoting matrix and pore can

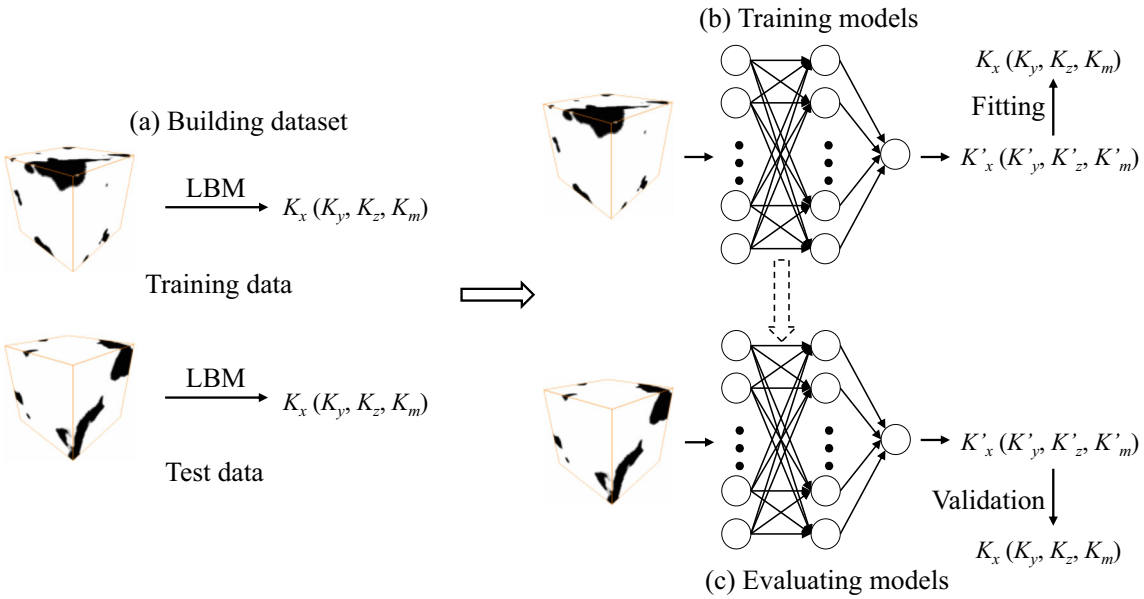

Fig. 1 Overview of research plan. K_x, K_y, K_z, and K_m represent the permeabilities computed by LBM. K'_x, K'_y, K'_z, and K'_m represent the permeabilities estimated by model

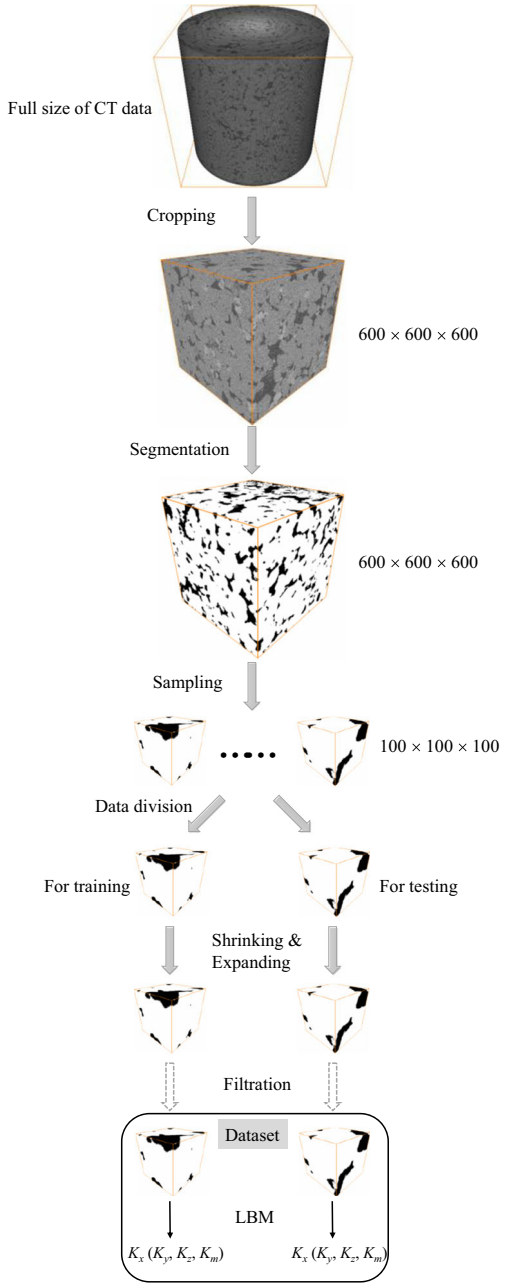

Fig. 2 Workflow of dataset acquisition

be counted, so the porosity was obtained and it is 14.7%. As shown in Fig. 2, the white and black of the binary image represent matrix and pore, respectively. The operations of cropping and segmentation were implemented on Avizo®, a general-purpose commercial software developed for scientific and industrial data visualization and analysis.

(ii) Sampling

After segmentation, a sliding window with size of 100 × 100 × 100 was utilized to sweep over the 600-cube binary image for sampling. The size of sliding window should be less than the size of representative volume element (RVE). RVE refers to the smallest cube which can represent the mechanical and hydrodynamic properties of the whole core sample [51, 52]. Generally, the samples with greater than or equal to the size of RVE have similar porosity and hydrodynamic property. Therefore, we recommend that the size of the sampling window should be smaller than the size of RVE, which makes the difference of porosity and permeability between subsamples large enough. The method of selecting the size of RVE can be found in Ref. [53]. For our core sample, RVE size is about 650 × 650 × 650 according to our analysis (not pictured) and 100 × 100 × 100 is smaller than the size of RVE obviously. Figure 3 gives a toy example for illustrating the sampling procedure. The shift step size was set to 50 voxels, so 1331 small cubes were obtained. These 100^3 small cubes can be considered as independent rocks [38]. Those samples were arbitrarily divided into two sets. One set contained 1265 samples for training, while the other set contained 66 samples (about 5%) for testing.

(iii) Shrinking and expanding

Basically, large-scale data is required for training a deep neural network having huge parameters. Therefore, data augmentation methods are extensively used in deep learning applications [54–56]. In this study, shrinking and expanding algorithms, which were originally developed for determining the percolation threshold, were employed as the data augmentation methods. The main aim of these two algorithms is to shrink or expand the pore space while keeping the structure similar to the original one. At here, we only give the illustration of shrinking algorithm (Fig. 4) and the expanding is the opposite. As Fig. 4a shows, the shrinking procedure can be illustrated as follows: the boundaries separating the pore and the surrounding solid move towards the pore with a given step size in three axial directions. More details about shrinking and expanding algorithms can be found in Ref. [49].

In addition to increasing the number of samples, employing shrinking and expanding algorithms has another purpose. Kozeny-Carman equation as the most famous semi-empirical formula in porous media seepage field reveals that porosity and SSA are particularly important for estimating

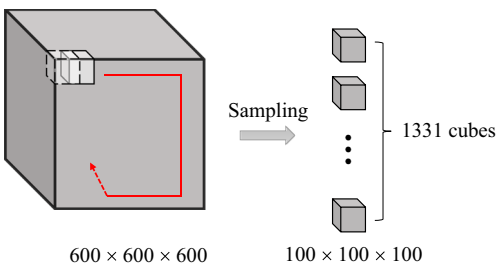

Fig. 3 A toy example of sampling. The white cube is the sliding window, and the red line is the moving path

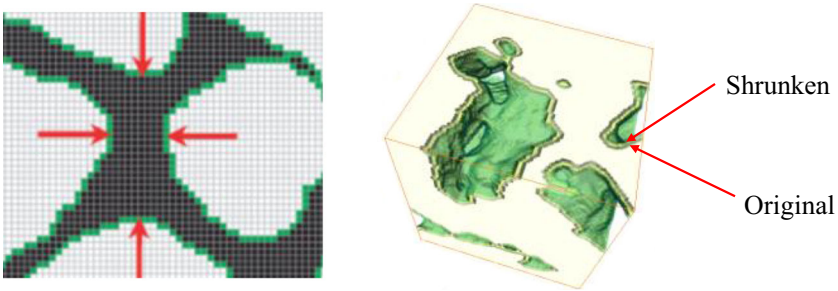

(a) 2D show of shrinking (b) An example of shrinking

Fig. 4 Illustration of shrinking algorithm. **a** The green lines denote the boundaries separating the pore (black) and the solid (white), and the red arrows denote the moving direction of the boundaries [49]. **b** The red arrows point to the original and shrunken boundaries

permeability [17, 18]. Ref. [37] also confirmed this point with reporting that physics-informed CNN, adding the two parameters of porosity and SSA into the input, outperformed regular CNN. In this study, we try to let the regular model itself learn the importance of porosity and SSA from the data instead of telling it directly. The largest differences in the geometry of the pores before and after shrinking or expanding are considered to be porosity and SSA, since both of them have almost the same morphology (Fig. 4b). Therefore, introducing some data generated by shrinking and expanding algorithms to training data is believed to make the model pay more attention to porosity and SSA during training.

All samples for training obtained from previous step were shrunken and expanded with step size of one, two, three, and four voxels respectively. Thus, total of 11,385 (1265 + 1265 × 4 (shrinking) + 1265 × 4 (expanding)) samples for training were obtained. Furthermore, the samples for testing were shrunken and expanded with step size of two voxels respectively, and 198 (66 + 66 × 1 (shrinking) + 66 × 1 (expanding)) samples were then obtained.

(iv) Filtration

We designed two rules to screen those samples for facilitating the experiments. Firstly, only the samples having porosity of 1 to 35% are chosen, covering the porosity values of most natural rocks. Secondly, only the samples having the pore geometries that connected in all three axes are selected, ensuring the permeabilities of each sample in three directions exist. This operation was implemented based on "CTSTA," an in-house Fortran program developed for analyzing and outputting of all clusters in the whole 3D binary image [57]. After screening, 4986 and 93 samples for training and testing respectively are retained (Table 1).

(v) Computation of permeability

In last decade, LBM, one of the most popular methods for pore-scale flow simulation, has been widely applied to explore the relationships between porosity and permeability in 3D pore geometries of sediments and rocks, acquired from stochastic or process-based reconstruction [58, 59], microCT imaging [3, 60–63], and focused ion beam nanotomography [64]. This is mainly because of the simplicity on solving the flow in complex pore geometries like natural rocks. Furthermore, parallel computing is easy to implement on LBM, facilitating handling relatively large volumes [65]. Thus, we employed direct pore-scale modeling with LBM to compute the permeability as the ground truth in this paper. In detail, the three-dimensional, nineteen-velocity (D3Q19) model [66] with single-relaxation time collision rule in combination with the bounce-back boundary rule was used in our experiments. All simulations were implemented on the fairly mature open-source lattice-Boltzmann library Palabos [67].

The computations are considered to be failed when one of the following two situations occurs in the numerical simulation processes. One is that the iteration process is divergent, and the other is that the convergence is too slow to exceed the set maximum number of iterations. The samples are retained only if the permeabilities in three axial directions are successfully computed in this study. Finally, a total of 3215 samples including 3158 for training and 57 for testing were obtained, each of which had three permeabilities (K_x, K_y, K_z) (see Table 1).

It is worth noting that those permeabilities were expressed in voxel squared since the inputs were voxel cubes, and they can be converted to the actual permeabilities (unit: *mD*) with physical meaning by the formula

$$K = k \cdot r^2 \cdot 1013.25 \left(1\mu m^2 = 1013.25 mD\right) \quad (1)$$

where K, k, and r denote the actual permeability, the permeability of voxel cube, and the resolution of the image (r = 1.9953 μm in our case).

For the flow and transport properties of anisotropic rocks, in addition to understanding the permeabilities in three axial directions of the rock, an indicator is needed to evaluate the overall permeability property of the rock so that the permeability of different anisotropic rocks can be compared. In this paper, we employed the geometric mean of the permeabilities in three axial directions as the indicator. The geometric mean is defined as

Table 1 Dataset distribution

Operation	Sampling	Shrinking and expanding	Screen	LBM (successful)
Training data	1265	11,385	4986	3158
Test data	66	198	93	57

$$K_m = \sqrt[3]{K_x \cdot K_y \cdot K_z}, \tag{2}$$

where K_x, K_y, and K_z represent the permeabilities in the direction of x-, y-, and z-axes respectively. K_m represents the mean permeability.

2.3 3D convolutional neural network

CNN inspired by human visual system is a modern branch of machine learning. Unlike traditional machine learning approaches which implement feature extraction, feature dimensionality reduction, and classification separately, CNN combines them as an end-to-end system, from raw images to the corresponding target values, avoiding manual design of appropriate features which is usually difficult. Basically, a typical CNN contains three kinds of commonly used neuronal layers which are convolution layer, pooling layer, and fully connected layer. Convolution layer is applied to extract the features, while pooling layer is used to reduce the features. Fully connected layer is employed as the classifier. As shown in Fig. 5, CNN stacks convolution layer and pooling layer alternately for achieving the task-related and low/mid/high-level features, and those features are then flattened into the fully connected layer for classification. Nowadays, although CNN has achieved remarkable successes in 2D image recognition tasks [54, 68, 69], it has been seldom extended to 3D image analyzing tasks.

(i) Convolution layer

Generally, convolution layer as the most important one consists of a set of small feature extractors (filters) with the same size but different weights, and all the weights can be learned during training. Those filters are applied to sweep over the input for achieving the feature maps [70]. In natural scenes, the input of 2D CNN is the image containing three color channels generally. In this regard, for handling the 3D input, the simplest way is to replace the color channels with the slices of the volumetric image. However, it is very different to use this scheme to process 3D data and directly process it with 3D CNN, and the detailed description is given in Fig. 6.

As Fig. 6a shows, given a 3D input with size of W (width) × H (height) × L (length), the input volume should firstly be split into L isolated slices along the length direction, and then those slices are fed into the 2D CNN. A filter containing L 2D convolution kernels is swept over the input along the red line path and do convolution calculations for achieving a 2D feature map. Since the kernels in filter are independent of each other, the feature map cannot capture the spatial information adequately along the third dimension (length direction), which means the encoded volumetric spatial information is partially lost [41].

However, it is crucial to extract features from all three dimensions and represent the volumetric image sufficiently for predicting the permeability in porous media. Therefore, 3D convolution kernel was applied to our task for capturing the spatial information in all three dimensions. As Fig. 6b shows, given the same 3D input with size of $W \times H \times L$, the entire volumetric image is inputted into the 3D CNN directly. A filter containing one 3D convolution kernel is employed to sweep over the whole volumetric image along the red line direction for generating a 3D feature map. The obtained feature map can take full advantage of the volumetric contextual information in all three dimensions.

Mathematically, the computational procedure of generating the activated feature maps can be briefly described as follows: (a) convolving the input with 3D convolution kernels and the feature maps; (b) adding a bias term to the convolution result; and (c) passing through a non-linear activation function for enhancing the ability of CNN to represent the non-linear features and accelerating the training process. The 3D convolution layer in an element-wise manner can be expressed as follow [71].

$$\boldsymbol{f}_j^i(w,h,l) = \boldsymbol{a}\left(\boldsymbol{b}_j^i + \sum_n \sum_{x,y,z} \boldsymbol{f}_n^{i-1}(w-x, h-y, l-z)\boldsymbol{K}^i(x,y,z)\right) \tag{3}$$

where $\boldsymbol{f}_j^i$ and $\boldsymbol{f}_n^{i-1}$ denote the jth 3D feature map in the ith layer and the nth 3D feature map in the (i-1)th layer respectively. $\boldsymbol{K}^i$

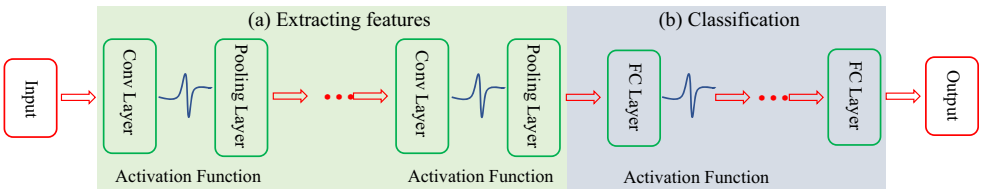

Fig. 5 Architecture of a typical CNN

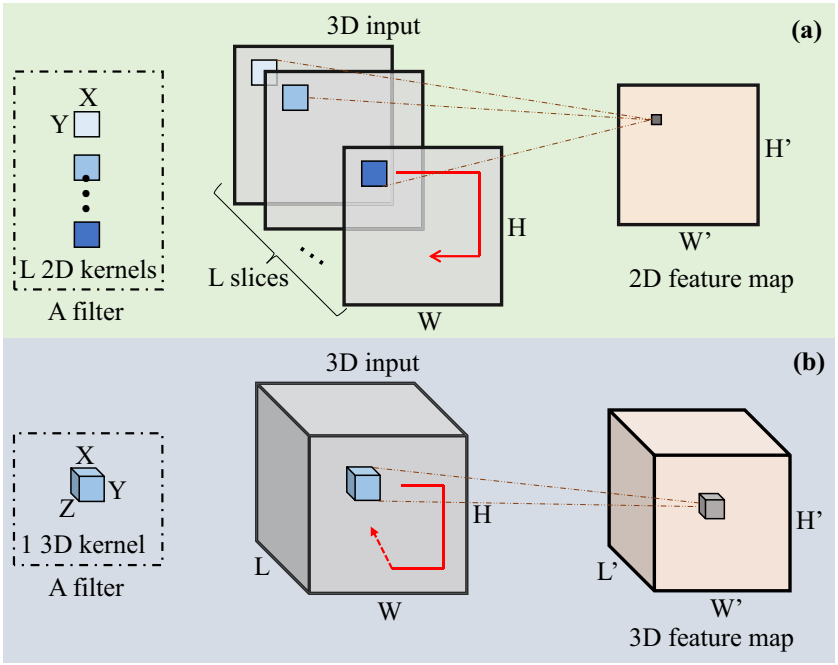

Fig. 6 Convolutional operations in 2D and 3D CNN for processing 3D input

and $\boldsymbol{b}_j^i$ denote the 3D convolution kernel and the bias term respectively. $\boldsymbol{a}(\cdot)$ represents the non-linear activation function. The rectified linear units (ReLU) [72] was employed as the activation function ($\boldsymbol{a}(x) = \max(0, x)$) in this paper.

Basically, the size of feature map is determined by the input size, kernel size, padding size, and stride size. As Fig. 6 shows, the 3D kernel with size of $X \times Y \times Z$ is employed to sweep over the 3D input with size of $W \times H \times L$, and then the 3D feature map with size of $W' \times H' \times L'$ is obtained. Suppose the padding size of the input is M and the stride size of the kernel is S. The feature map size is defined as follow [73].

$$W' = \frac{2M + W - X}{S} + 1 \tag{4}$$

$$H' = \frac{2M + H - Y}{S} + 1 \tag{5}$$

$$L' = \frac{2M + L - Z}{S} + 1 \tag{6}$$

(ii) Pooling layer

Because of the large number of features acquired by convolution layer, pooling layer is used to perform features reduction. As a non-linear down-sampling method, pooling operation can enhance the non-linear expression ability of CNN, reduces the computational burden, and avoids overfitting. Furthermore, it can help CNN resist the effect of slight translation, particularly conducing to image recognition. In this paper, max pooling strategy [74], selecting the largest element in each pooling region, was employed. Suppose there is a feature map $\boldsymbol{f}$ as the input of the pooling layer. A set of small local regions $\boldsymbol{R}$ is applied to generate a pooled feature map $\boldsymbol{P}$ as the output. Its definition is given as [75].

$$\boldsymbol{P}_j = \max_{i \in \boldsymbol{R}_j} \boldsymbol{f}_i, \tag{7}$$

where $\boldsymbol{R}_j$ stands for the jth pooling region in the feature map $\boldsymbol{f}$, and i stands for the index of each element in this pooling region.

(iii) Fully connected layer

After the input passes through several convolution and pooling layers, a stack of 3D feature maps representing the 3D input is obtained. Fully connected layer is applied to perform high-level reasoning to those features for classification. In fully connected layers, each neuron in current layer is connected with all neurons in the neighbor layers, producing the densest connections and learnable parameters in the network. The detailed implementation process can be expressed as follows: (a) flattening the 3D feature maps into a feature vector as the input of fully connected layer; (b) multiplying the input with a vector-matrix of weights; (c) adding a bias term to the multiplication result; and (d) employing a non-linear function to generate the activations. Fully connected layer is formulated as the following equation [71].

$$\boldsymbol{f}^i = \boldsymbol{a}\left(\boldsymbol{b}^i + \boldsymbol{W}^i \boldsymbol{f}^{i-1}\right) \tag{8}$$

where $\boldsymbol{f}^{i-1}$ and $\boldsymbol{f}^i$ stand for the input feature vector outputted from the (i-1)th layer and the output vector of the ith layer,

respectively; $\boldsymbol{W}^i$, $\boldsymbol{b}^i$, and $\boldsymbol{a}(\cdot)$ represent the weight matrix, the bias term, and the non-linear activation function (ReLU), respectively.

2.4 Evaluation metrics

In this paper, three commonly used metrics were employed to evaluate the performance of the surrogate models proposed for rapid estimation of permeability in anisotropic rock. They are coefficient of determination (R^2), root mean squared error (RMSE), and standard deviation (Std), and the corresponding definitions are given as

$$R^2 = 1 - \frac{\sum_{i=1}^{m}\left(y_i - \widehat{y}_i\right)^2}{\sum_{i=1}^{m}\left(y_i - \overline{y}\right)^2}, \tag{9}$$

$$\mathrm{RMSE} = \sqrt{\frac{1}{m}\sum_{i=1}^{m}\left(y_i - \widehat{y}_i\right)^2}, \tag{10}$$

$$\mathrm{Std} = \sqrt{\frac{\sum_{j=1}^{n}\left(x_j - \overline{x}\right)^2}{n-1}}, \tag{11}$$

where y_i and $\overline{y}$ denote the ith observation and the mean of all observations respectively, $\widehat{y}_i$ denotes the ith fitted value, m is the number of observations, x_j and $\overline{x}$ denote the jth value and the mean of those values respectively, and n is their number.

3 Experiment results

3.1 Dataset statistics

Deep learning is a data-driven machine learning algorithm, which means that the quality of the model depends strongly on the feeding data. Therefore, it is quite important to give detailed information about training data and test data, which will provide important reference for readers to repeat the experiment. In view of this, we conducted a detailed statistical analysis on the obtained training data and test data in this section, shown in Figs. 7, 8, and 9.

Figure 7 gives the porosity distributions of the training data and the test data. The porosity of training data reaches the peak value (near 19%) in the middle and decreases symmetrically on both sides. Comparatively, the porosity distribution of test data does not show regularity, and most of those porosities roughly evenly distributed between 10 and 27%. Although the distributions of training data and test data differ greatly, the averages and standard deviations of the two sets of data are basically the same.

Figure 8 shows the permeability distributions of the training data and the test data. As Fig. 8a, c, e, and g show, in training data, the permeabilities in the direction of x-, y-, and z-axes and the mean permeability are left skewed distribution on logarithmic coordinate. Among those permeabilities, the mean permeability has the smallest average and standard deviation, which indicates the mean permeability is densely concentrated near the average, showing the least volatility. The permeabilities in the direction of x- and y-axes have the largest standard deviation and average, respectively. In terms of test data, shown in Fig. 8b, d, f, and h, all kinds of the permeability are left skewed distribution on logarithmic coordinate. Similar to training data, the mean permeability of test data also has the smallest average and standard deviation. The permeability in the direction of x-axis has the largest standard deviation and average, denoting the greatest volatility.

Figure 9 offers the relationship between the permeability and the porosity in training data. Comparing to the permeabilities in the direction of x-, y-, and z-axes, the mean permeabilities are more concentrated as a whole. The distributions of all kinds of permeability look like cloud of points, but the permeabilities with higher porosity are bigger than that with lower porosity from the whole, showing a certain correlation between porosity and permeability. This fact indicates that the porosity is important for estimating the permeability in our dataset, confirming the necessity of making the 3D CNN models pay more attention to porosity.

Furthermore, to investigate the relationship between the anisotropy ratio and the porosity in training data, we defined the anisotropy ratio r as Eq. (12) [76]. $K_{\min}$, K_{int}, and $K_{\max}$ denote the minimum, intermediate, and the maximum permeability, respectively. As the equation shows, the range of anisotropy ratio is 0 to1. The smaller the r, the higher the degree of anisotropy. Figure 10 gives the relationship of the anisotropy ratio and the porosity. As Fig. 10 shows, there is no significant correlation between porosity and anisotropy of samples. The distribution of anisotropy degree of all samples is fairly uniform.

$$r = \frac{K_{\min}}{\sqrt{K_{\mathrm{int}} K_{\max}}} \tag{12}$$

3.2 Structure of 3D CNN

In this paper, we proposed four 3D CNN-based models sharing the network structure for rapidly estimating the permeabilities in three axial directions and the mean permeability. The detailed structure of the designed 3D CNN is given in Table 2. In our experiments, all the weights of network were initialized randomly. Mean squared error was employed as the loss function since the task of the network is regression, and the commonly used stochastic gradient descent (SGD) [77] with momentum of 0.9 was applied to optimize it. The hyperparameters were tuned with grid search method for

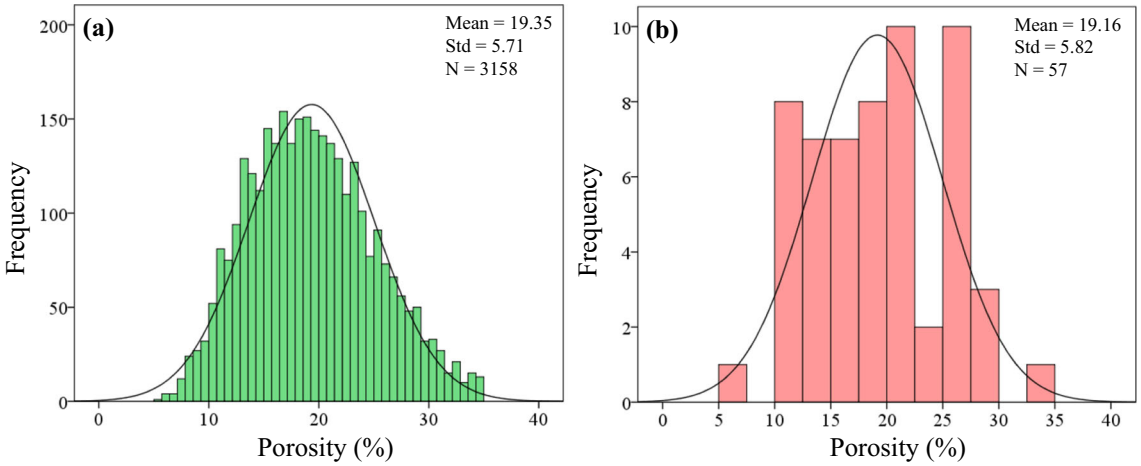

Fig. 7 Porosity distributions of training data (**a**) and test data (**b**). Mean is the arithmetic average of samples, and *N* is their number

achieving the best performance. The epoch and mini batch were set to 20 and 8, respectively. The global learning rate was set to 0.002 and decreased to 90% per 10 epochs.

3.3 Performances of 3D CNN

This section shows the performances of our approach on fitting and predicting the permeabilities of natural sandstone in three axial directions. Three surrogate models based on 3D CNN were proposed, corresponding to the three kinds of permeability. It should be noted that those models have the same network structure (Table 2) but different weights. In order to evaluate the performances of those models quantitatively, R^2 score and RMSE were employed. These two indicators assess the difference between the permeability estimated by the trained model and the permeability computed by LBM (ground truth).

In terms of training, as Table 3 shows, the permeabilities in training data in all axial directions were fitted quite well by our models and the performances of these models are almost the same according to the R^2 scores and RMSEs. It indicates that the 3D CNN can describe the relationship between the 3D geometry of pore space and the permeability in the training data quite well. At the same time, it shows that the structure of the designed 3D CNN is reasonable and suitable for all three kinds of permeability.

In our experiments, the weights of network were initialized randomly and the random seed was not fixed, leading to randomness of predictions. Therefore, it is necessary to perform multiple times on each model for ensuring the reliability of the results. In this paper, we ran 10 times and average the ten predictions as the final result. The prediction results are shown in Table 3 and Fig. 11.

As Table 3 shows, all the models achieved fairly high R^2 scores which are greater than 0.82, indicating that all the proposed models have satisfactory prediction performances. The models of *x*- and *y*-axes got almost the same R^2 scores and RMSEs, which means that the predictive effects of them are the same basically. In terms of the model of *z*-axis, although its R^2 score is the worst, its RMSE is the lowest. This should be because the permeability in z-axis direction has the smallest standard deviation and average (see Fig. 8b, d, and f).

In order to assess the stability of ten predicted values on each sample, the standard deviation was employed. As the error bars in Fig. 11 show, the standard deviations increase with the increase of the predicted values except for a few points, which means that the larger the true value to be predicted, the larger the fluctuation range of the multiple predicted values of the model.

In Fig. 11, it is found that most of the true data fall within the standard deviation of the predicted data, which means the predicted data can basically fit the true data. Actually, most of the predicted values are smaller than the true values, especially the permeability in the *y*-axis direction. For quantitatively assessing the differences between those predicted values and those true values as a whole, two dashed lines denoting the averages of the true values and the predicted values were added to the Fig. 11. As we can see in Fig. 11a–c, all averages of the predicted values are smaller than that of the true values, 14.39%, 28.94%, and 16.75% smaller respectively, which means that the overall prediction deviation in the *y*-axis direction is the largest.

3.4 Prediction of mean permeability

To predict mean permeability, two methods are available. One is to build a model containing one 3D CNN having the same structure but different weights with the above three models for predict the mean permeability (Fig. 12a). Same process as predicting the permeabilities in three axial directions, we can obtain the predicted mean permeability by inputting the 3D binary image, which represents pore geometry, to this model. The other

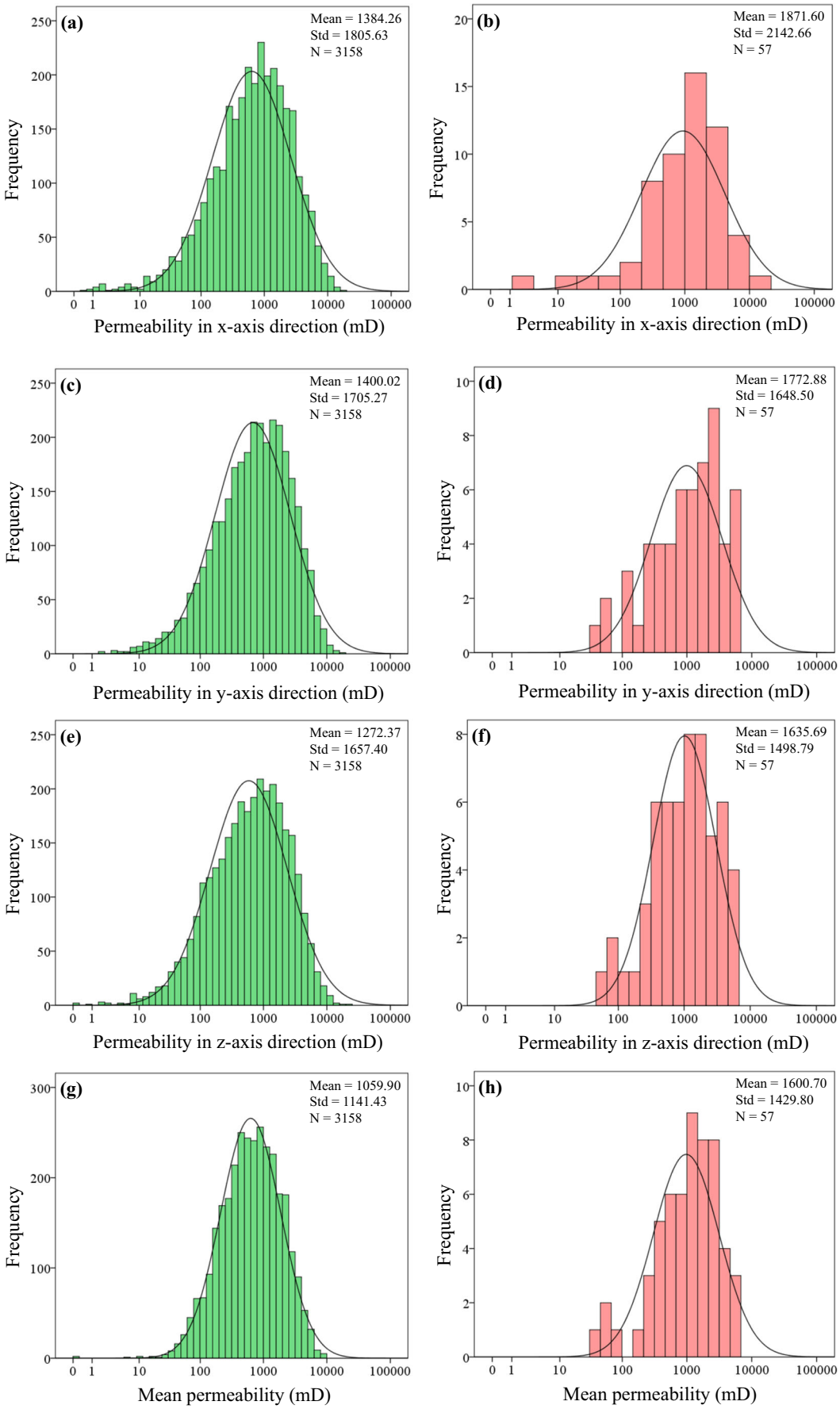
(a)
Mean = 1384.26
Std = 1805.63
N = 3158
Frequency
Permeability in x-axis direction (mD)
(b)
Mean = 1871.60
Std = 2142.66
N = 57
Frequency
Permeability in x-axis direction (mD)
(c)
Mean = 1400.02
Std = 1705.27
N = 3158
Frequency
Permeability in y-axis direction (mD)
(d)
Mean = 1772.88
Std = 1648.50
N = 57
Frequency
Permeability in y-axis direction (mD)
(e)
Mean = 1272.37
Std = 1657.40
N = 3158
Frequency
Permeability in z-axis direction (mD)
(f)
Mean = 1635.69
Std = 1498.79
N = 57
Frequency
Permeability in z-axis direction (mD)
(g)
Mean = 1059.90
Std = 1141.43
N = 3158
Frequency
Mean permeability (mD)
(h)
Mean = 1600.70
Std = 1429.80
N = 57
Frequency
Mean permeability (mD)

◀ **Fig. 8** Permeability distributions of the training data and the test data. **a**, **c**, **e**, and **g** The permeabilities of training data, respectively. **b**, **d**, **f**, and **h** The permeabilities of test data

one is to calculate the geometric mean of the permeabilities in three axial directions predicted above. It is obvious that the latter method is equivalent to building a model combination consisting of three CNNs to predict the mean permeability (Fig. 12b).

Based on the above two methods, two sets of the predicted mean permeability were obtained. One set predicted by the single model achieved a quite good prediction result with a R^2 score of 0.9155 and a RMSE of 761.1174. The other set predicted by the model combination achieved a similar prediction result with a R^2 score of 0.8907 and a RMSE of 623.9015. It is obvious that both methods show good performance according to the R^2 score and RMSE.

More detailed information on these prediction results is shown in Fig. 13. It is found that both predicted values gained by single model and model combination are smaller than the true values in most cases, showing the same trend as predicting the permeabilities in three axial directions. Compared with the single model, most of the predicted values achieved by the model combination are larger than that achieved by the single model, closer to the true values. The averages of them, showing with dashed lines in Fig. 13, indicate that the overall prediction deviation of the model combination is smaller.

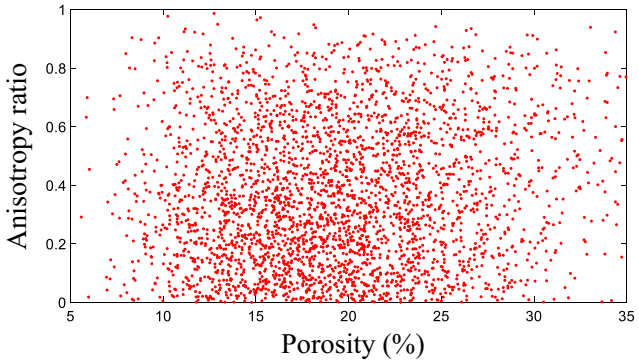

Fig. 10 Relationship between the anisotropy ratio and the porosity in training data

3.5 Generalization evaluation

In the above, our training data and test data are taken from the same rock specimen (Coconino sandstone). Although the structure of samples in the training and test data are quite different from each other, some potential similar characteristics existed in the same rock may facilitate the prediction accuracy. Therefore, it is necessary to compute the permeability of one or more separate sandstone image dataset using the trained 3D CNN for evaluating the generalization ability of the model.

For this goal, we collected a Bentheim sandstone with porosity of 23.7%. Bentheim sandstone is Lower Cretaceous and originates from Bentheim, Germany [50]. Since the workflow of data acquisition is quite similar to Section 2.2, here we briefly introduce the data collection work. The Bentheim sandstone was X-ray CT scanned with the resolution of 5.001 μm. The obtained

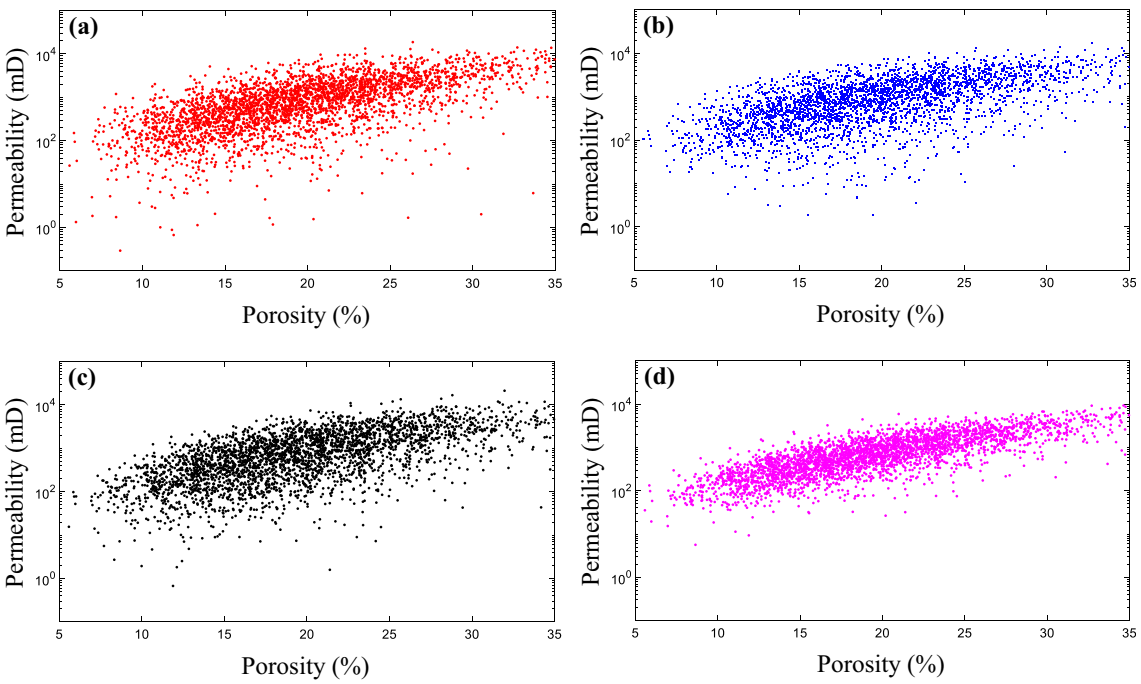

Fig. 9 Relationship between the permeability and the porosity in training data. **a**–**d** The permeabilities in the direction of *x*-, *y*-, and *z*-axes, and the mean permeabilities, respectively

Table 2 The proposed 3D CNN architecture

Layer type	Setting	Feature map
Input		100(width) × 100(height) × 100(length) × 1(channels)
Conv_layer	32(out channels), 5(kernel size), 1(stride), 2(padding)	100 × 100 × 100 × 32
Pooling_ layer	5 (kernel size), 5 (stride), 0 (padding)	20 × 20 × 20 × 32
Conv_layer	64, 5, 1, 2	20 × 20 × 20 × 64
Pooling_ layer	5, 5, 0	4 × 4 × 4 × 64
Conv_layer	128, 3, 1, 1	4 × 4 × 4 × 128
Pooling_ layer	4, 4, 0	1 × 1 × 1 × 128
FC_layer	64 (weights) × 128, 64 (bias) × 1	1 × 1 × 1 × 64
FC_layer	32 × 64, 32 × 1	1 × 1 × 1 × 32
FC_layer	1 × 64, 1 × 1	1 × 1 × 1 × 1

3D CT image was cropped and segmented with an appropriate threshold (Fig. 14). A 3D binary volume with size of 500 × 500 × 500 representing the pore geometry was obtained. A sliding window with size of 100 × 100 × 100 was utilized to sweep over the 500-cube binary image with step size of 100 for generating 125 samples. Samples with porosity below 1% and over 35% were removed. The permeabilities of the samples with porosity of in three directions were computed with LBM method as the ground truth. Finally, only 104 samples with permeabilities in all three axis directions were retained.

The permeability of those Bentheim samples were predicted using the proposed 3D CNN trained on the training data of Coconino sandstone. All results are average on 10 runs. We computed the R^2 and the RMSE between the predicted permeabilities and the corresponding ground truth, giving in Table 4. As Table 4 shows, the prediction results are good according to the R^2 and the RMSE, showing good generalization ability. However, the prediction accuracy of permeabilities of Bentheim sandstone in all three axis directions is lower than that of Coconino sandstone, as shown in Table 3 and Table 4.

3.6 Evaluation of computation time

In our experiments, we performed all the numerical simulations on Tianhe-2 (also called Milkyway-2) for computing the permeabilities in three axial directions. Tianhe-2 supercomputer

Table 3 Performances of fitting and predicting the permeabilities in three axial directions

CNN model	R^2		RMSE (mD)	
	Training	Test	Training	Test
X-axis	0.9799	0.8972	300.6881	900.2870
Y-axis	0.9738	0.8821	281.7957	892.9472
Z-axis	0.9796	0.8201	291.8665	705.2174

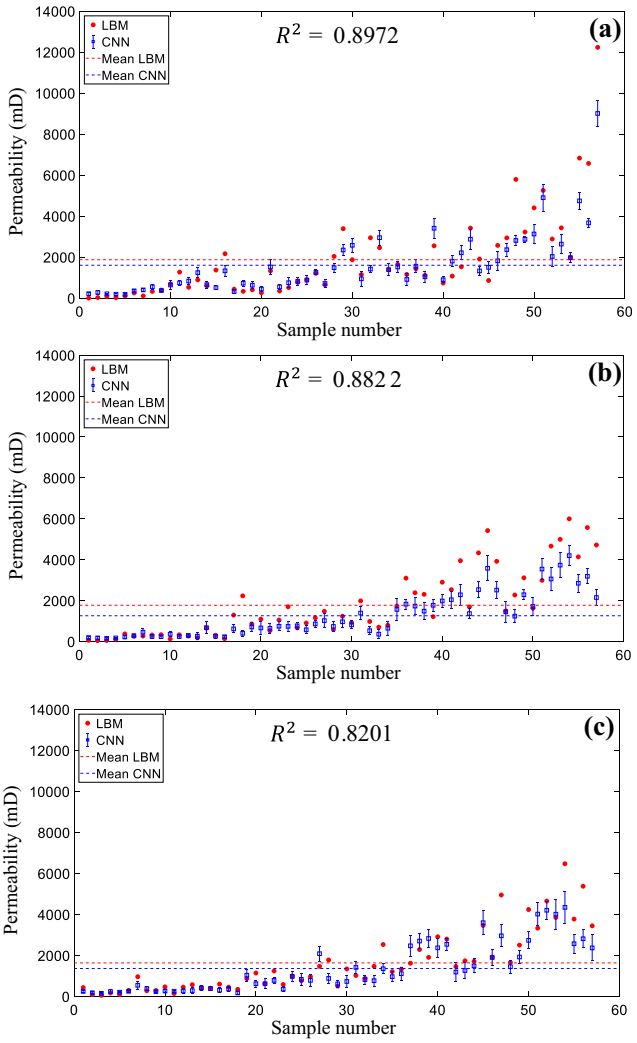

Fig. 11 Prediction results of the permeabilities in three axial directions. **a**–**c** The permeabilities in the direction of *x*-, *y*-, and *z*-axes, respectively. The error bar represents the average and standard deviation of the prediction results over 10-run. The red dashed line named "Mean LBM" and blue dashed line named "Mean CNN" as the reference denote the averages of the true values and the predicted values, respectively

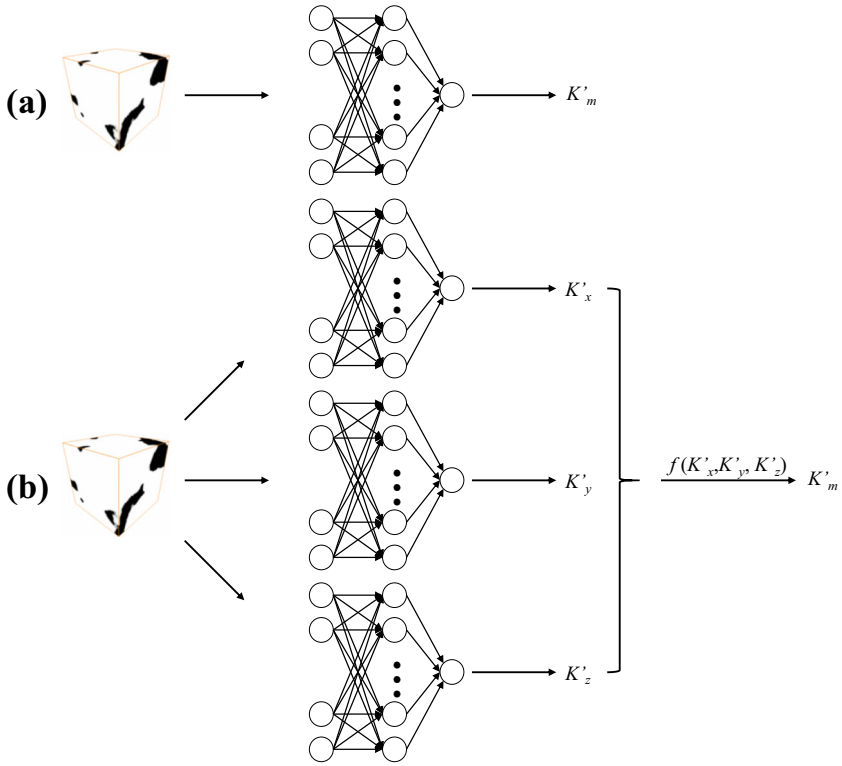

Fig. 12 Workflows of two methods for predicting the mean permeability. "$f(\,)$" denotes the geometric mean function

equipped with Intel Xeon CPUs and Intel Xeon Phi accelerators is one of the most powerful supercomputers in the world [78]. We applied for 3 nodes on Tianhe-2 to calculate the permeabilities in three axial directions respectively, and enabled 24 cores for parallel computing on each node. Finally, it took about 38 days to calculate the permeabilities of all samples including 4986 samples for training and 93 samples for testing. A total of 3215 samples including 3158 for training and 57 for testing were retained. On average, about 646.43 s are required to calculate the permeability of one sample with size of 100 × 100 × 100 in one axial direction.

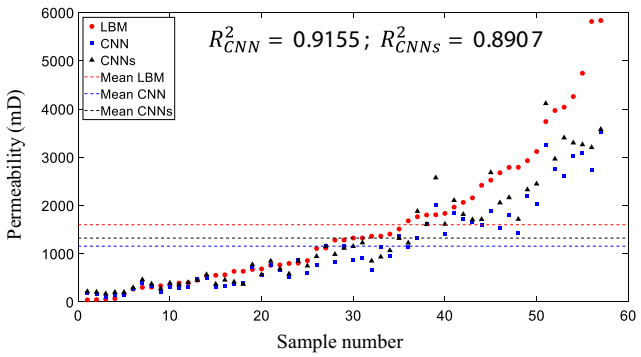

Fig. 13 Estimation results of the mean permeability via single model and model combination containing three CNNs. R^2_{CNN} and R^2_{CNNs} stand for the R^2 scores of single model and model combination respectively. The red dashed line named "Mean LBM" represents the average of the true values, while the blue dashed line named "Mean CNN" and black dashed line named "Mean CNNs" represent the averages of the predicted values gained by single model and model combination, respectively

In terms of predicting the permeability, we built the 3D CNN on the fairly mature deep learning framework: PyTorch 0.4.1. All training and prediction experiments were implemented on a personal computer. The personal computer is equipped with i9-9900k CPU, 16.0 GB RAM, and NVIDIA GeForce RTX 2080 Ti GPU. After training the 3D CNN with training data, about 3.33 s were took to predict all 57 testing samples by using the trained model. On average, about 58.42 ms are required to predict the permeability of one sample in one axial direction, which means the time taken by the LBM method to compute the permeability is 11,065 times that of 3D CNN.

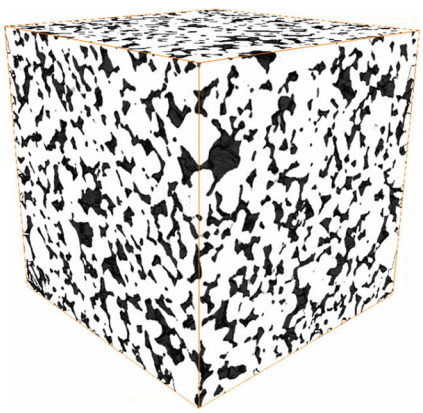

Fig. 14 The pore geometry of Bentheim sandstone. The white and black of the binary image denote matrix and pore, respectively

Table 4 Accuracy of the 3D CNN trained on Coconino sandstone in predicting permeability of Bentheim sandstone

CNN model	R^2	RMSE (mD)
X-axis	0.6623	2007.110
Y-axis	0.7221	2953.313
Z-axis	0.6979	3061.386

4 Discussion

Applying scientific knowledge to the data-based science models can further improve their performances [79]. Inspired by this, Wu et al. [37] improved the performance of CNN for predicting the permeability of synthetic two-dimensional porous media by combining image information (the artificial 2D image representing pore geometry) and integral quantities (SSA and porosity). However, when predicting the permeability of a new sample with the model obtained by this method, it is necessary to calculate the SSA and porosity of the sample in advance, leading to the trouble of manual intervention. In order to make the model pay more attention to these two parameters and build an end-to-end framework, shrinking and expanding algorithms were employed to generate training data (see Section 2.2). This is a way to change the focus of model learning by adjusting the proportion of sample types covered by training data. With this trick, we obtained the desired prediction results on the permeabilities in three axial directions and the mean permeability (see Fig. 11 and Fig. 13).

In the prediction results, it is found that the predicted values of all kinds of permeability are smaller than the true values in most cases, leading to overall low prediction results. In response to this phenomenon, we give a possible explanation here. Taking the prediction result of the permeability in the *x*-axis direction as an example, as can be seen from Fig. 8a, the number of the samples with permeability of around 900 in training data is the largest, which may bias the predicted values of the model near this value. On the other hand, as Fig. 8a and b, from the average of the training data and the test data, the distribution of the former is lower than the latter, which may lead to a lower overall distribution of the predicted values outputted by the model. The above two facts resulted in the predicted values are lower than the true values as a whole.

For predicting the mean permeability, we utilized two kinds of model (see Fig. 12) and both of them obtained satisfactory prediction results (see Fig. 13). The single model achieved a higher R^2 score, while the model combination gained smaller RMSE and overall prediction deviation. The performance of these two models can be considered as the same roughly because of their gap on the three indicators are not large. However, we still recommend the single model in this paper since it has a higher R^2 score, reflecting a stronger correlation between the predicted values and true values.

For performing generalization evaluation, we predicted the permeability of Bentheim sandstone using the 3D CNN trained on the training data of Coconino sandstone. The predictions of Bentheim sandstone are not as good as that of the test data of Coconino sandstone (Table 4). That should be because the training data is Coconino sandstone only. This phenomenon may indicate that the samples taken from the rock of the same type may have some potential similar characteristics. Those similar characteristics may make the prediction result better to some extent. Ideally, the rock types covered by the test data need to be included in the training data, so that the predictions of test data can achieve the best accuracy.

Nowadays, although numerous numerical simulation methods have been developed for computing permeability accurately, those methods have high computational complexity and are time consuming. Therefore, Kozeny-Carman equation, the most famous semi-empirical formula in porous media seepage field, is usually employed to estimate the permeability in actual production. Kozeny-Carman equation describes the relationship between permeability and a limited number of low-level features designed by human, such as porosity, specific surface area, tortuosity, fractal exponent. As the development of imaging technology, it is practical to obtain high-resolution digital 3D images of rocks. Extracting a limited number of low-level features from these images is a great waste of information. Compared with Kozeny-Carman equation, the convolution layer in CNN can automatically extract task-related and high-level features, easy to scale up to other types of porous media. At the same time, the fully connected layer in CNN can provide excellent approximation of the most ideal function describing the relationship between permeability and those obtained features if this function exists, which is obviously superior to the formula of Kozeny-Carman equation obtained from experience. Furthermore, the 3D CNN-based approach estimates the permeability is also very fast, more than 10,000 times faster than LBM in our experiments (see Section 3.5). Therefore, we think that the CNN-based approach is a comprehensive upgrade of the Kozeny-Carman equation, having great potential in practical applications. More importantly, Kozeny-Carman equation cannot take the anisotropy of rock permeability into account since the parameters in it are not directional. Except for estimating the absolute permeability, it is possible to extend the CNN-based approach to multiphase fluid permeability and other properties which only relate to the geometry of pore space.

5 Conclusion

In this paper, we proposed a 3D CNN-based approach for rapidly estimating the permeability in natural anisotropic rock. In acquiring dataset, shrinking and expanding algorithms were employed to increase the number of samples and make the model pay more attention to porosity and specific surface area (SSA) for further improving performance. Four models

sharing the same network structure were designed for predicting the permeabilities in three axial directions and the mean permeability, respectively. We obtained the satisfactory prediction results of the permeabilities in *x*-, *y*-, and *z*-axis directions and the mean permeability with high R^2 scores. Furthermore, the designed models also achieved good generalization ability in predicting the permeability of other samples.

In the future, quantitatively evaluating the impact of shrinking and expanding algorithms on the prediction results will be performed for optimizing the proportion of the samples generated by shrinking or expanding algorithms in training data. More different types of rocks covered by the training data set will be collected for enhancing the prediction accuracy. Furthermore, we will apply the 3D CNN-based approach to predicting other fluid flow properties and mechanical properties of rocks.

Acknowledgments Thanks to Dr. Ma Xiaodong for providing microCT images of sandstone samples.

Funding information This paper is supported by the National Natural Science Foundation of China (41574087).

Compliance with ethical standards

Conflict of interest The authors declare that there are no conflicts of interest.

References

1. Blunt, M.J., et al.: Pore-scale imaging and modelling. Adv. Water Resour. **51**, 197–216 (2013)
2. Wildenschild, D., Sheppard, A.P.: X-ray imaging and analysis techniques for quantifying pore-scale structure and processes in subsurface porous medium systems. Adv. Water Resour. **51**, 217–246 (2013)
3. Andrä, H., et al.: Digital rock physics benchmarks—part II: computing effective properties. Comput. Geosci. **50**, 33–43 (2013)
4. Bultreys, T., De Boever, W., Cnudde, V.: Imaging and image-based fluid transport modeling at the pore scale in geological materials: a practical introduction to the current state-of-the-art. Earth Sci. Rev. **155**, 93–128 (2016)
5. Gingold, R.A., Monaghan, J.J.: Smoothed particle hydrodynamics: theory and application to non-spherical stars. Mon. Not. R. Astron. Soc. **181**(3), 375–389 (1977)
6. Chen, S., Doolen, G.D.: Lattice Boltzmann method for fluid flows. Annu. Rev. Fluid Mech. **30**(1), 329–364 (1998)
7. Martys, N.S., Chen, H.: Simulation of multicomponent fluids in complex three-dimensional geometries by the lattice Boltzmann method. Phys. Rev. E Stat. Phys. Plasmas Fluids Relat. Interdiscip. Topics. **53**(1), 743–750 (1996)
8. Kandhai, D., et al.: A comparison between lattice-Boltzmann and finite-element simulations of fluid flow in static mixer reactors. Int. J. Mod. Phys. C. **9**(08), 1123–1128 (1998)
9. Meakin, P. and Tartakovsky, A. M.: Modeling and simulation of pore-scale multiphase fluid flow and reactive transport in fractured and porous media. Rev. Geophys.. **47**(3) (2009)
10. Koroteev, D., et al.: Direct hydrodynamic simulation of multiphase flow in porous rock. Petrophysics. **55**(04), 294–303 (2014)
11. Yang, J., Crawshaw, J., Boek, E.S.: Quantitative determination of molecular propagator distributions for solute transport in homogeneous and heterogeneous porous media using lattice Boltzmann simulations. Water Resour. Res. **49**(12), 8531–8538 (2013)
12. Yoon, H., Kang, Q., Valocchi, A.J.: Lattice Boltzmann-based approaches for pore-scale reactive transport. Rev. Mineral. Geochem. **80**(1), 393–431 (2015)
13. Joekar-Niasar, V., et al.: Trapping and hysteresis in two-phase flow in porous media: a pore-network study. Water Resour. Res. **49**(7), 4244–4256 (2013)
14. Blunt, M.J.: Flow in porous media — pore-network models and multiphase flow. Curr. Opin. Colloid Interface Sci. **6**(3), 197–207 (2001)
15. Vogel, H.J., Roth, K.: Quantitative morphology and network representation of soil pore structure. Adv. Water Resour. **24**(3), 233–242 (2001)
16. Sok, R.M., et al.: Direct and stochastic generation of network models from tomographic images; effect of topology on residual saturations. Transp. Porous Media. **46**(2), 345–371 (2002)
17. Kozeny, J.: Vber kapillare leitung des wassers im boden. Sitzungsber Akad. Wiss. Wien. **136**(2a), 271–306 (1927)
18. Carman, P.C.: Permeability of saturated sands, soils and clays. J. Agric. Sci. **29**(2), 262–273 (1939)
19. Xu, P., Yu, B.: Developing a new form of permeability and Kozeny–Carman constant for homogeneous porous media by means of fractal geometry. Adv. Water Resour. **31**(1), 74–81 (2008)
20. Ozgumus, T., Mobedi, M., Ozkol, U.: Determination of Kozeny constant based on porosity and pore to throat size ratio in porous medium with rectangular rods. Eng Appl Comput Fluid Mech. **8**(2), 308–318 (2014)
21. Cybenko, G.: Approximation by superpositions of a sigmoidal function. Math. Control Signals Syst. **2**(4), 303–314 (1989)
22. Hornik, K.: Approximation capabilities of multilayer feedforward networks. Neural Netw. **4**(2), 251–257 (1991)
23. Sonoda, S., Murata, N.: Neural network with unbounded activation functions is universal approximator. Appl. Comput. Harmon. Anal. **43**(2), 233–268 (2017)
24. Shaham, U., Cloninger, A., Coifman, R.R.: Provable approximation properties for deep neural networks. Appl. Comput. Harmon. Anal. **44**(3), 537–557 (2018)
25. Hong, J., et al.: Classification of cerebral microbleeds based on fully-optimized convolutional neural network. Multimed. Tools Appl., (2018)
26. Hong, J., et al.: Improvement of cerebral microbleeds detection based on discriminative feature learning. Fund Inform. **168**(2–4), 231–248 (2019)
27. Wang, S.-H., Hong, J. and Yang, M.: Sensorineural hearing loss identification via nine-layer convolutional neural network with batch normalization and dropout. Multimed. Tools Appl. (2018)
28. Hong, J., et al.: Detecting cerebral microbleeds with transfer learning. Mach. Vis. Appl. (2019)
29. Wang, S.-H., et al.: Alcoholism identification via convolutional neural network based on parametric ReLU, dropout, and batch normalization. Neural Comput. & Applic. (2018)
30. Zhang, Y., et al.: Adaptive convolutional neural network and its application in face recognition. Neural. Process. Lett. **43**(2), 389–399 (2016)
31. Wu, Y., et al.: Deep Convolutional Neural Network with Independent Softmax for Large Scale Face Recognition, in Proceedings of the 24th ACM International Conference on Multimedia, ACM: Amsterdam, The Netherlands. p. 1063–1067 (2016)
32. Guo, S., Chen, S., and Li, Y.: Face recognition based on convolutional neural network and support vector machine. in

2016 IEEE International Conference on Information and Automation (ICIA). (2016)
33. Cecen, A., et al.: Material structure-property linkages using three-dimensional convolutional neural networks. Acta Mater. **146**, 76–84 (2018)
34. Yang, Z., et al.: Deep learning approaches for mining structure-property linkages in high contrast composites from simulation datasets. Comput. Mater. Sci. **151**, 278–287 (2018)
35. Cang, R., et al.: Improving direct physical properties prediction of heterogeneous materials from imaging data via convolutional neural network and a morphology-aware generative model. Comput. Mater. Sci. **150**, 212–221 (2017)
36. Mosser, L., Dubrule, O., Blunt, M.J.: Reconstruction of three-dimensional porous media using generative adversarial neural networks. Phys. Rev. E. **96**(4), 043309 (2017)
37. Wu, J., Yin, X., Xiao, H.: Seeing permeability from images: fast prediction with convolutional neural networks. Sci. Bull. **63**(18), 53–60 (2018)
38. Sudakov, O., Burnaev, E., Koroteev, D.: Driving digital rock towards machine learning: predicting permeability with gradient boosting and deep neural networks. Comput. Geosci. **127**, 91–98 (2019)
39. Urban, G., et al.: Multi-modal brain tumor segmentation using deep convolutional neural networks. MICCAI BraTS (Brain Tumor Segmentation) Challenge. Proceedings, winning contribution: p. 31–35 (2014)
40. Turaga, S.C., Murray, J.F., Jain, V., Roth, F., Helmstaedter, M., Briggman, K., Denk, W., Seung, H.S.: Convolutional networks can learn to generate affinity graphs for image segmentation. Neural Comput. **22**(2), 511–538 (2010)
41. Dou, Q., et al.: Automatic detection of cerebral microbleeds from MR images via 3D convolutional neural networks. IEEE Trans. Med. Imaging. **35**(5), 1182–1195 (2016)
42. Zewei, D., et al.: Investigation of different skeleton features for CNN-based 3D action recognition. in 2017 IEEE International Conference on Multimedia & Expo Workshops (ICMEW). (2017)
43. Kim, J., et al.: Learning spectro-temporal features with 3D CNNs for speech emotion recognition. in 2017 Seventh International Conference on Affective Computing and Intelligent Interaction (ACII). IEEE (2017)
44. Wu, M., Xiao, F., Johnson-Paben, R.M., Retterer, S.T., Yin, X., Neeves, K.B.: Single-and two-phase flow in microfluidic porous media analogs based on Voronoi tessellation. Lab Chip. **12**(2), 253–261 (2012)
45. Newman, M.S., Yin, X.: Lattice Boltzmann simulation of non-Darcy flow in stochastically generated 2D porous media geometries. SPE J. **18**(01), 12–26 (2013)
46. Yong, Y., et al.: Direct simulation of the influence of the pore structure on the diffusion process in porous media. Comput. Math. Appl. **67**(2), 412–423 (2014)
47. Stauffer, D., Aharony, A.: Introduction to percolation theory. Taylor & Francis, London (1992)
48. Liu, J., Pereira, G.G., Regenauer-Lieb, K.: From characterisation of pore-structures to simulations of pore-scale fluid flow and the upscaling of permeability using microtomography: a case study of heterogeneous carbonates. J. Geochem. Explor. **144**, 84–96 (2014)
49. Liu, J., Regenauer-Lieb, K.: Application of percolation theory to microtomography of structured media: percolation threshold, critical exponents, and upscaling. Phys. Rev. E. **83**(1), 016106 (2011)
50. Ma, X., Haimson, B.C.: Failure characteristics of two porous sandstones subjected to true triaxial stresses. J. Geophys. Res. Solid Earth. **121**(9), 6477–6498 (2016)
51. Terada, K., et al.: Simulation of the multi-scale convergence in computational homogenization approaches. Int. J. Solids Struct. **37**(16), 2285–2311 (2000)
52. Pelissou, C., et al.: Determination of the size of the representative volume element for random quasi-brittle composites. Int. J. Solids Struct. **46**(14), 2842–2855 (2009)
53. Liu, J., et al.: Improved Estimates of Percolation and Anisotropic Permeability from 3-D X-Ray Microtomography Using Stochastic Analyses and Visualization. Geochem. Geophys. Geosyst.. **10**(5) (2009)
54. Krizhevsky, A., Sutskever, I., Hinton, G.E.: ImageNet classification with deep convolutional neural networks. Commun. ACM. **60**(6), 84–90 (2017)
55. Wang, S., et al.: Cerebral micro-bleed detection based on the convolution neural network with rank based average pooling. IEEE Access. **5**, 16576–16583 (2017)
56. Wang, S.-H., Lv, Y.D., Sui, Y., Liu, S., Wang, S.J., Zhang, Y.D.: Alcoholism detection by data augmentation and convolutional neural network with stochastic pooling. J. Med. Syst. **42**(1), 2 (2017)
57. Liu, J., et al.: Applications of microtomography to multiscale system dynamics: visualisation, characterisation and high performance computation. In: Yuen, D.A., et al. (eds.) GPU Solutions to Multi-scale Problems in Science and Engineering, pp. 653–674. Springer Berlin Heidelberg, Berlin (2013)
58. Keehm, Y., Mukerji, T., and Nur, A.: Permeability prediction from thin sections: 3D reconstruction and Lattice-Boltzmann flow simulation. Geophys. Res. Lett.. **31**(4) (2004)
59. Wu, K., et al.: 3D stochastic modelling of heterogeneous porous media – applications to reservoir rocks. Transp. Porous Media. **65**(3), 443–467 (2006)
60. Manwart, C., et al.: Lattice-Boltzmann and finite-difference simulations for the permeability for three-dimensional porous media. Phys. Rev. E. **66**(1), 016702 (2002)
61. Fredrich, J. T., DiGiovanni, A. A., and Noble, D. R.: Predicting macroscopic transport properties using microscopic image data. J. Geophys. Res. Solid Earth. **111**(B3) (2006)
62. Khan, F., et al.: 3D simulation of the permeability tensor in a soil aggregate on basis of nanotomographic imaging and LBE solver. J. Soils Sediments. **12**(1), 86–96 (2012)
63. Shah, S.M., et al.: Micro-computed tomography pore-scale study of flow in porous media: effect of voxel resolution. Adv. Water Resour. **95**, 276–287 (2016)
64. Yoon, H., Dewers, T.A.: Nanopore structures, statistically representative elementary volumes, and transport properties of chalk. Geophys. Res. Lett. **40**(16), 4294–4298 (2013)
65. Talon, L., et al.: Assessment of the two relaxation time Lattice-Boltzmann scheme to simulate Stokes flow in porous media. Water Resour. Res.. **48**(4) (2012)
66. Qian, Y.H., Orszag, S.A.: Lattice BGK models for the Navier-Stokes equation: nonlinear deviation in compressible regimes. Europhys Lett. **21**(3), 255–259 (1993)
67. Tan, J., Sinno, T.R., Diamond, S.L.: A parallel fluid–solid coupling model using LAMMPS and Palabos based on the immersed boundary method. J. Comput. Sci. **25**, 89–100 (2018)
68. Szegedy, C., et al.: Going deeper with convolutions. in 2015 IEEE Conference on Computer Vision and Pattern Recognition (CVPR). (2015)
69. He, K., et al.: Deep residual learning for image recognition. in 2016 IEEE Conference on Computer Vision and Pattern Recognition (CVPR). (2016)
70. Lecun, Y., et al.: Gradient-based learning applied to document recognition. Proc. IEEE. **86**(11), 2278–2324 (1998)
71. Dou, Q., Chen, H., Yu, L., Qin, J., Heng, P.A.: Multilevel contextual 3-D CNNs for false positive reduction in pulmonary nodule detection. IEEE Trans. Biomed. Eng. **64**(7), 1558–1567 (2017)
72. Nair, V. and Hinton, G. E.: Rectified linear units improve restricted boltzmann machines, in Proceedings of the 27th International Conference on International Conference on Machine Learning, Omnipress: Haifa, Israel. p. 807-814 (2010)

73. Hong, J. and Liu, J.: Cerebral microbleeds detection via convolutional neural network with and without batch normalization, in Frontiers in Intelligent Computing: Theory and Applications, Springer. p. 152–162 (2020)
74. Boureau, Y.-L., Ponce, J., and LeCun, Y.: A theoretical analysis of feature pooling in visual recognition. in Proceedings of the 27th international conference on machine learning (ICML-10). (2010)
75. Zeiler, M.D. and Fergus, R.: Stochastic pooling for regularization of deep convolutional neural networks. arXiv preprint arXiv: 1301.3557. (2013)
76. Clavaud, J.-B., et al.: Permeability anisotropy and its relations with porous medium structure. J. Geophys. Res. Solid Earth. **113**(B1) (2008)
77. Ketkar, N.: Stochastic gradient descent, in Deep Learning with Python: A Hands-on Introduction, Apress: Berkeley, CA. p. 113-132 (2017)
78. Che, Y., et al.: Petascale scramjet combustion simulation on the Tianhe-2 heterogeneous supercomputer. Parallel Comput. **77**, 101–117 (2018)
79. Karpatne, A., et al.: Physics-guided neural networks (pgnn): an application in lake temperature modeling. arXiv preprint arXiv: 1710.11431. (2017)